minerals

MDPI

Article

Mineralogy, Geochemistry and Stable Isotope Studies of the Dopolan Bauxite Deposit, Zagros Mountain, Iran

Somayeh Salamab Ellahi [1], Batoul Taghipour [1,*], Alireza Zarasvandi [2], Michael I. Bird [3] and Alireza K. Somarin [4]

[1] Department of Earth Sciences, Shiraz University, Shiraz 7146713565, Iran; somayesalamat@yahoo.com
[2] Department of Geology, Earth Sciences Faculty, Shahid Chamran University, Ahvaz 6135743136, Iran; zarasvandi_a@scu.ac.ir
[3] College of Science, Technology and Engineering, Centre for Environmental and Sustainability Science, James Cook University, PO Box 6811, Cairns, Queensland 4870, Australia; michael.bird@jcu.edu.au
[4] Department of Geology, Faculty of Sciences, Brandon University, Brandon, MB R7A 6A9, Canada; somarina@brandonu.ca
* Correspondence: taghipour@shirazu.ir; Tel.: +98-713-613-7457

Academic Editor: Maria Economou-Eliopoulos
Received: 10 November 2015; Accepted: 28 January 2016; Published: 6 February 2016

Abstract: The Dopolan deposit is a Mediterranean-type bauxite located in the Zagros Fold-Thrust Zone, Iran. This deposit consists of five lithological members including iron-rich, clay-rich, oolitic, pisolitic and organic matter-containing bauxites. The mineralogy of the deposit includes diaspore, boehmite, and kaolinite, nacrite, with minor pyrite, anatase and rutile. Geochemical studies show that light rare earth elements (LREEs) are enriched relative to heavy rare earth elements (HREEs) in all members, supporting an authigenic origin. Mass changes based on Ti as an immobile element indicate that conventionally-immobile elements (Al, Nb, Ta, Zr, Hf) are enriched *in situ* in the residual units, whereas mobile elements (K, Ca, Si) were depleted during bauxitization. This study shows that the Khaneh–Kat argillitic dolomite is the likely parent rock. The $\delta^{18}O$ (7.63‰ to 9.35‰) and δD values (−49.91‰ to −66.49‰) for kaolinite in the bauxite samples suggest equilibration with meteoric waters which supports a supergene origin. Bauxitization occurred in a warm climate with relatively constant isotopic composition suggesting climate stability during the development of bauxite horizons and remobilization of Al (with formation of secondary boehmite). The $\delta^{13}C$ values of calcite (−7.3‰) in the bauxite support the idea that the Khaneh–Kat Formation has experienced post-depositional isotope exchange with meteoric waters during the karstification process.

Keywords: karst bauxite; stable isotope; Dopolan; Zagros; Iran

1. Introduction

Residual and concealed bauxites are two important sedimentary aluminum deposits. Residual bauxite deposits are classified as karst bauxite and laterite type bauxite [1]. Karst bauxite deposits from the Mediterranean region and other worldwide bauxite formations have been investigated by a number of authors [2–11]. Karst bauxite genesis is related to paleo-weathering products derived from different rocks types including carbonate rocks, marl, volcanic and magmatic rocks [12–17].

Karst bauxite deposits are commonly characterized by high content of Al_2O_3, TiO_2, high field strength elements (HFSE), and abundant detrital minerals such as zircon, tourmaline and rutile [11,18,19]. The mobility and behavior of elements during bauxitization have also been discussed by a number of researchers [8,11,14,17–22]. To investigate mobility of elements in weathered systems, various methods have been discussed by some researchers [10,14,23–25]. Formation of bauxite horizons

in the Phanerozoic was a climate dependent process; it has been established that the Phanerozoic bauxites were generally formed in hot or warm humid climates [26]. These conditions allowed intensive weathering of carbonate rocks, karstification and subsequent bauxite development [26].

Stable isotopes (H, C and O) have been used to study bauxite genesis and indirectly determine paleo-environments associated with its formation [27]. The $\delta^{18}O$ and δD values of minerals such as kaolinite, goethite, gibbsite and boehmite can be used to deduce information about the conditions that prevailed during bauxitization [28]. Hydrogen isotope ratios may be affected by post-formation isotope exchange with meteoric water at low surficial temperature or higher temperatures as a result of diagenetic conditions [29]. Carbon isotope composition of organic matter can indicate the role of microbial activity during deposition and mineralization of carbonate which may reflect environmental conditions and biogeochemical processes that controlled the formation of bauxite [30].

The most important known bauxite deposits in Iran are distributed in four regions, namely: (1) Sanandaj–Sirjan belt, Permo–Triassic and late Triassic in Bukan and Kanshiteh; (2) The Zagros Fold belt, Upper Cretaceous, Triassic in Mandan, Deh-now, Sarfaryab and Dopolan [9]; (3) The Alborz mountains, Upper Triassic in Tilabad and Jajarm [31]; and (4) The central plateau of Iran, Upper Triassic, Permo-Triassic in Bazargan and Balbaloyeye [31] (Figure 1).

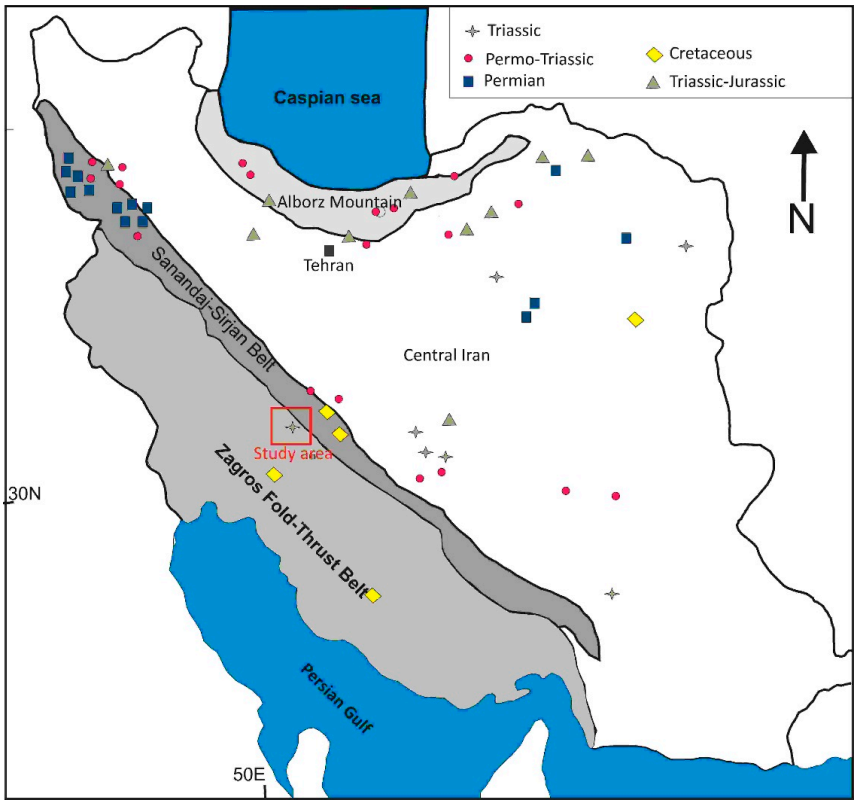

Figure 1. Schematic map of Iran with location of the Zagros Fold Belt, Alborz Mountain, Central Iran, and distribution of bauxite deposits.

The Triassic Dopolan bauxite deposit is located in the Chaharmahal and Bakhtiary province in a high Zagros structural zone. The Dopolan bauxite deposit has an estimated reserve of 8–15 million tons with an average grade of 45% Al_2O_3 [32]. Previous studies of the Dopolan bauxite deposit show that the bauxite formed as a continental deposit filling karstic cavities at the boundary of the Khaneh–Kat and Neyriz Formations [33]. The aim of this study is to determine the precursor rock and understand the bauxitization process during formation of this deposit. To attain these objectives,

detailed geological, mineralogical, petrographical and geochemical investigations (including ^{18}O and D isotopes) were carried out and the results are discussed here.

2. Geology

The Dopolan deposit is located in the High Zagros thrust zone near the border of Zagros and Central Iran zones. The structural framework of the thrust zone is complex, with significant folding and faulting. The Zagros fold belt evolved during the collision event between the Arabian and Eurasian plates [34] during late Cretaceous [35] and Pliocene [36].

The Zagros orogenic/metallogenic belt extends from the Turkish–Iranian border in NW to the Makran zone in SE Iran [37]. This belt consists of five tectonically related parallel zones: Zagros simple folded belt, the "Crushed zone" or High Zagros, the Main Zagros thrust, the Sanandaj–Sirjan zone, and the Urumieh–Dokhtar magmatic arc [38]. The High Zagros is characterized by earlier deformation, large offsets on basement faults, steep contacts with surrounding zones and more ductile deformation [39] (Figure 1). The geomorphology of the Dopolan area is characterized by many mountain peaks, up to 2200 m high separated by deep valleys. The Dopolan bauxite is located in a large structure called the Sabzkuh–Kelar Synclinorium, which is bounded by two thrust faults. In the studied area, the Zagros stratigraphy consists of Cambrian to Quaternary sequences. The oldest strata are located on limbs and youngest rocks in the core of sycnclinorium, uplifted by faults [32].

In the Dopolan deposit, the lithostratigraphic column includes pinkish Permian dolomite (Dalan Formation) at the base, overlain by the Upper Triassic argillitic dolomite (Khaneh–Kat Formation), and Jurassic dolomite (Neyriz Formation) (Figure 2).

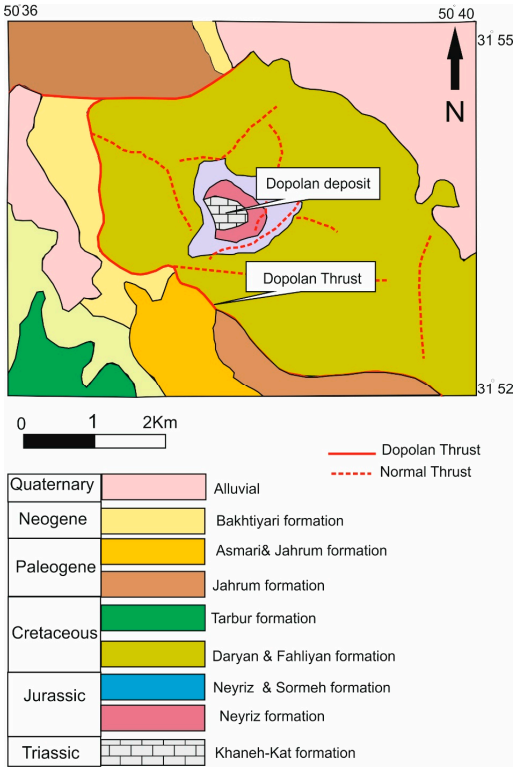

Figure 2. Geological map of the Dopolan bauxite deposit [40].

Argillite and bauxite ore layers lie above the Triassic brecciated argillitic dolomite (Figure 3A). The Khaneh–Kat Formation is predominantly composed of dolostone and marly limestone with a matrix of calcite (Figure 3B) [41]. This formation consists of a massive crystalline and porous dolomite at the top with more clay-rich carbonates and shale in the lower parts [42]. The

Khaneh–Kat Formation is intensely karstified with bauxite filled karst and caves (sinkholes) at the top of the Khaneh–Kat Formation (Figure 3C,D). Karstification in the Khaneh–Kat Formation is the result of specific paleo-climatic regimes as climate and time are important to the development of extensive karst landforms [43]. The studied deposits are situated along a disconformity between the Khaneh–Kat and Neyriz Formations, implying extended periods of subaerial exposure (karstification, weathering, bauxitization).

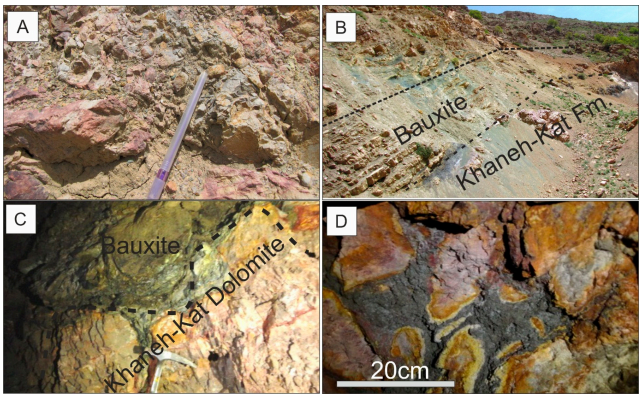

Figure 3. Field photograph of various karst features in the Upper Khaneh–Kat Formation: (**A**) Brecciated argillite; (**B**) Bauxite horizon and relationship with the Khaneh–Kat Formation (footwall dolomite); (**C**) Iron-rich bauxite-filled sinkhole in karst in the Khaneh–Kat Formation; (**D**) Karstified footwall filled with iron-rich bauxite detritus.

The main bauxite horizon occurs at the contact of the Khaneh–Kat and Neyriz Formations where bauxite-filled paleo-sinkholes in the Khaneh–Kat Formation. The main bauxite horizon is composed of five distinct layers including (from bottom to top): iron-rich, clay-rich, oolitic (powdery white bauxite), pisolitic and organic-rich (black) bauxite layers (Figure 4).

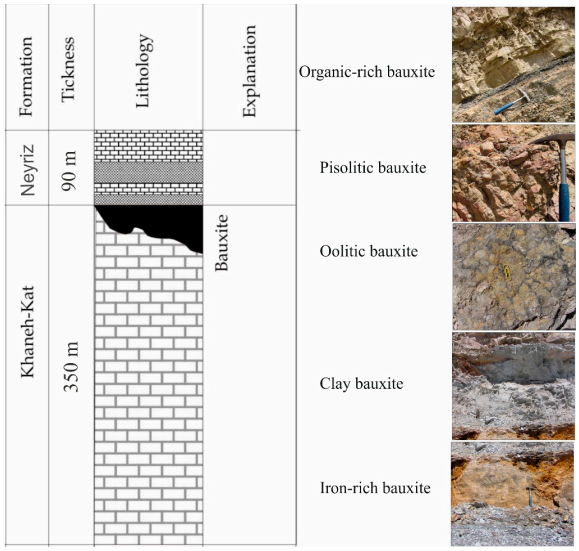

Figure 4. Schematic profile of the Dopolan bauxite deposit; on the right diverse bauxite facies.

The lower part of the bauxite horizon is comprised of iron-rich bauxite, ~1.5 m thick, which directly overlies the Khaneh–Kat Formation. The mineral assemblage of this unit is pyrite, kaolinite and boehmite [44]. Clay-rich, oolitic and pisolitic bauxite layers are intercalated between the iron-rich bauxite at the base and organic-rich bauxite at the top. The clay-rich bauxite, ~5 m thick, has grey to

light grey color and shows fine-grained oolitic texture. It is the main ore zone with 53% Al_2O_3, 2% TiO_2. Kaolinite, diaspore, boehmite and quartz as main minerals [32]. Field evidence such as presence of plant root casts show that the deposit formed in a marsh sedimentary basin. The clay-rich bauxite is overlain by the oolitic bauxite which is characterized by a vuggy structure, fine-grained (0.4–5 mm) oolitic texture, low density, with mineralogy dominated by diaspore and boehmite. Pisolitic bauxite, 0.5–3 m thick, overlies the oolitic bauxite. This layer contains 1–5 cm dark grey hard concretions with abundant diaspore and an average of 70% Al_2O_3, 3% Fe_2O_3 and 2% TiO_2 [32]. The transition between the upper pisolitic bauxite and the lower part of the black organic-rich bauxite is gradual and indistinct. The average thickness of the organic-rich bauxite is 1.20 m with kaolinite, a small amount of nacrite and rutile, and abundant plant remnants, which are locally converted to small lenses or thin coal layers.

3. Methodology

Field investigations were carried out over two periods (2013–2014) during which 60 specimens were sampled from the bauxite quarry and argillite (Khaneh–Kat Formation). Thirty-four samples of the five identified bauxite horizons were selected for petrographic studies. A detailed mineralogical analysis of the bauxite samples was performed by X-Ray diffraction (XRD) at the Geological Survey of Iran (Tabriz center) using a Philiphs X pert Step-Tro Model D-5000 diffractometer (Philiphs, Amsterdam, The Netherlands) with Co Kα (1.789 Å) radiation, fixed graphite monochromators, voltage 40 kV current 30 mA, 0.02 step size, scan range 4°–80°, drive axis 2θ. Major and trace element content in the representative samples were obtained using inductively coupled plasma mass spectrometry (ICP-MS) in the Acme Analytical Laboratories, Vancouver, BC, Canada. Sample preparation was based on digestion of 0.2 g sample in lithium metaborate flux and fusion in a furnace at 1000 °C. The melt is then dissolved in 100 mL diluted HCl acid.

Before isotopic measurement, samples were crushed with mortar and pure minerals were separated using the method of Bird *et al.* (1992) [45]. Stable isotope analysis was carried out at Cornell Isotope Laboratory in the United States. Isotope ratios were determined using a high precision Thermo Delta V isotope ratio mass spectrometer (Bremen, Germany) interfaced to a Temperature Conversion Elemental Analyzer (TC/EA). Analyses were performed utilizing several in-house and commercial standards for internal checks on instrument accuracy and precision. Results for $\delta^{18}O$ were compared against the Vienna Standard Mean Ocean Water (V-SMOW) [46]. Carbon isotope values reported in standard δ notation in units of per mil (‰) relative to the [46] Vienna Peedee Belemnite standard. The $\delta^{13}C$ values were reproducible to $\pm$0.2‰.

4. Mineralogy

Mineralogical and textural investigations based on optical microscopy and XRD analysis show that diaspore, kaolinite and nacrite are the main mineral components in the bauxite horizons with boehmite, anatase, rutile and muscovite as minor phases (Table 1). Diaspore is the dominant Al mineral found in the Dopolan bauxite. The matrix, authigenic in origin, shows predominantly pelitomorphic, microgranular and panidiomorphic textures; however, there are also some terrigenous grains such as intraclasts, ooids and erosional ooid nucleus which suggest an allochthonous origin for some components of the deposit. In addition, pelitomorphic and fluidal textures in this deposit suggest allochthonous bauxitization of the parent rock. This may be due to insufficient speed to remove dissolved silica that led to the kaolinite formation.

Two forms of pyrite occur in bauxite horizons: framboidal pyrite and euhedral pyrite (Figure 5A,B). Framboidal pyrite commonly forms during early diagenesis under organic-rich, anoxic conditions [7,11,47,48]. Euhedral pyrite occurs as cubic grain filling fractures and is interpreted to have formed during the last stages of diagenesis. Petrographic observations show the fragments in the central part of the pisolites are filled with the secondary porous matrix composed of kaolinite (Figure 5C,D). The pisolitic bauxite is characterized by the presence of pisolitic textures. Microscopic

investigation suggests two pisolite forms: (1) simple pisolites with a kaolinite core surrounded by a preserved cortex of boehmite (Figure 5E); (2) complex residual rounded fragments typical of pisolitic bauxite, so called allogenic pisolites (Figure 5D) [49]. Micromorphological evidence such as pisolites with simple, complex and oolitic cores indicate that deposit can be divided into two types—autochthonous and allochthonous (Figure 5C–E).

Table 1. X-Ray diffraction (XRD) mineralogical results and textural characteristics of selected samples of the Dopolan deposit.

Sample No.	Bauxite Layers	Matrix	Major Phases	Minor Phases
Do-IR	Iron-rich bauxite	Panidiomorph	Nacrite, Kaolinite, Pyrite	Anatase, Boehmite, Muscovite (< 10%), Rutile
Do-Cl	Clay-rich bauxite	Microgranular	Kaolinite, quartz, Diaspore	Boehmite
Do-Oo	Oolitic bauxite	unknown	Diaspore, Nacrite	Anatase, Muscovite (< 10%), Rutile
Do-Pi	Pisolitic bauxite	Macrocrystalline	Diaspore	Anatase, Nacrite, Muscovite, Rutile
Do-Org	Organic-rich bauxite	unknown	Nacrite, Kaolinite, Pyrite	Anatase, Rutile
Kha	Dolomite, Khane kat	unknown	Calcite, Dolomite, Montmorillonite	-

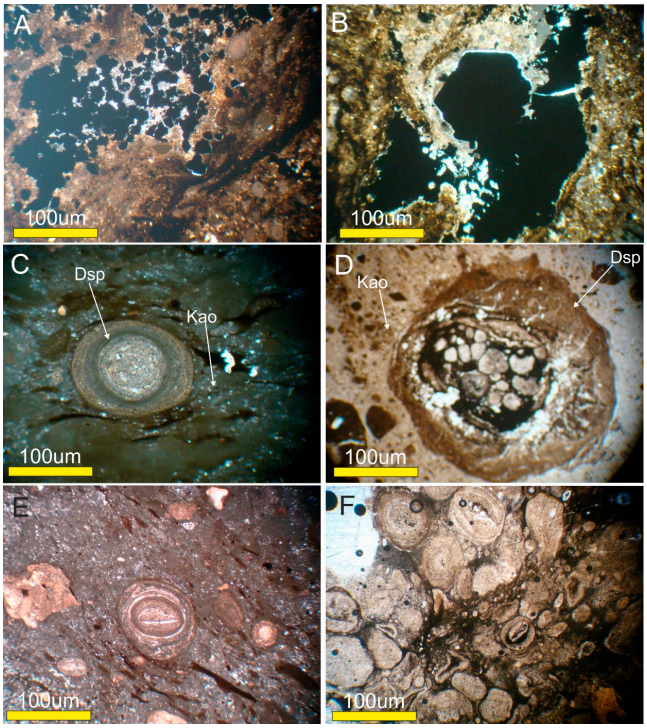

Figure 5. Microphotographs of the Dopolan deposit: (**A**) Euhedral and framboidal pyrite in the iron-rich bauxite; (**B**) Euhedral pyrite in the organic-rich bauxite; (**C**) Diaspore concretion in a porous matrix composed of kaolinite; (**D**) Complex residual rounded fragments typical of pisolitic bauxite; (**E**) Simple pisolite with a kaolinite core surrounded by a preserved cortex of boehmite; (**F**) Discolored pisolites showing deferrification process, kao = kaolinite, Dsp = diaspore.

5. Geochemistry

5.1. Major and Trace Elements

Whole rock major, trace and rare earth element (REE) analyses of bauxite horizons are provided in Table 2. The average of Al_2O_3 content of the Dopolan bauxites varies between 26 wt % and

72 wt %, while the average content of Fe_2O_3 and SiO_2 commonly ranges between 1 wt % and 17 wt % and 1 wt % and 35 wt %, respectively (Table 2).

Table 2. Major and trace element compositions of samples from the Dopolan deposit, Khaneh–Kat and Neyriz Formations. Detection limits for major and trace elements are 0.002% and 0.05 ppm, respectively.

Major Element (wt %)	Samples								
	Do-IR-1	**Do-IR-2**	**Do-IR-3**	**Do-IR-4**	**Do-Cl-1**	**Do-Cl-2**	**Do-Oo-1**	**Do-Oo-2**	**Do-Oo-3**
SiO_2	7.21	16.14	14.62	11.25	35.28	31.87	7.44	5.68	5.63
Al_2O3	42.02	31.34	37.58	47.1	47.39	50.69	68.11	67.78	68.23
Fe_2O_3	19.68	21.08	16.42	11.18	2.59	1.02	3.53	2.47	4.55
CaO	0.06	0.10	0.04	0.13	0.06	0.05	0.07	0.11	0.04
K_2O	0.51	1.16	0.61	0.85	0.80	0.36	0.30	0.65	0.80
MnO	0.01	0.02	0.01	0.00	0.00	0.00	0.00	0.00	0.00
Na_2O	0.01	0.01	0.01	0.06	0.01	0.01	0.01	0.02	0.01
P_2O_5	0.10	0.09	0.08	0.07	0.06	0.07	0.10	0.07	0.09
MgO	0.28	0.58	0.36	0.42	0.10	0.28	0.05	0.41	0.10
TiO_2	1.47	1.07	1.75	1.50	1.92	2.38	2.15	2.35	2.35
LOI	26.3	25.9	28.13	26.32	11.27	12.62	17.35	20.36	16.89
Sum	97.64	97.48	99.62	98.88	99.47	99.35	99.12	99.89	98.69
Trace Element (ppm)	**Samples**								
	Do-IR-1	**Do-IR-2**	**Do-IR-3**	**Do-IR-4**	**Do-Cl-1**	**Do-Cl-2**	**Do-Oo-1**	**Do-Oo-2**	**Do-Oo-3**
Ni	340	394	345	382	296	289	236	150	111
Cr	429	286	577	381	359	255	486	442	389
Ba	12	20	18	30	6	26	8	8	10
Hf	6.6	6.5	13.6	9.7	8.9	14.8	12.2	9.9	18.9
Th	24.5	25.7	34.3	36.2	21.5	49.6	44.5	28.4	46.3
Zr	246	250	340.1	364	271	583	419	308	557
Nb	43.1	35.3	46.2	38.3	45.6	54.4	52.6	54.7	77.7
S	>5	>5	>5	>5	1	2.1	1.4	1.5	2.5
Sr	413	342	450	408	423	542	517	567	552
Ta	4.6	3.9	6.2	2.7	4.4	5	5.3	5.2	7.2
Major Element (wt %)	**Samples**								
	Do-Oo-4	**Do-Pi-1**	**Do-Pi-2**	**Do-Pi-3**	**Do-Org-1**	**Do-Org-2**	**Khaneh–Kat**		**Neyriz**
SiO_2	3.20	4.67	5.45	3.11	34.84	35.44	1.09		0.32
Al_2O_3	72.89	74.98	73.25	75.09	31.1	26.55	0.39		1.42
Fe_2O_3	0.92	2.26	2.33	1.36	5.52	7.45	0.74		4.16
CaO	0.03	0.04	0.08	0.07	0.90	0.13	34.32		35.11
K_2O	1.21	0.25	1.64	0.29	4.06	3.83	0.11		0.86
MnO	0.00	0.00	0.00	0.02	0.03	0.00	0.01		0.04
Na_2O	0.07	0.01	0.04	0.06	0.05	0.12	0.03		0.03
P_2O_5	0.08	0.13	0.12	0.15	0.06	0.05	0.02		0.02
MgO	0.24	0.02	0.03	0.34	0.32	0.91	19.81		18.87
TiO_2	2.65	2.83	2.34	2.77	0.95	0.94	0.04		0.12
LOI	17.82	15.42	15.67	16.56	22.67	23.24	43.05		39.85
Sum	99.11	100.62	100.96	99.82	100.50	98.66	99.59		100.79
Trace Element (ppm)	**Samples**								
	Do-Oo-4	**Do-Pi-1**	**Do-Pi-2**	**Do-Pi-3**	**Do-Org-1**	**Do-Org-2**	**Khaneh–Kat**		**Neyriz**
Ni	273	220	258	170	407	270	33.2		25.1
Cr	329	132	139	303	747	1088	26		19
Ba	30	10	-5	13	46	37	12		6
Hf	17.7	16.9	15.5	17.8	5.3	6.2	0.2		0.7
Th	51.9	38.6	38.7	54.7	10.6	17.3	0.6		1.7
Zr	535.8	467.2	437.8	478.4	206	132	5.9		27.8
Nb	67.9	41.4	28.4	62.4	38.2	33.8	3.8		4.4
S	1.7	1.2	1.4	1.2	2.2	1.7	1.5		1.7
Sr	486	254	187	446	325	345	81.6		51.8
Ta	8.1	5.6	3.1	6.4	3.6	2.9	0.2		0.2

LOI = Loss or Ignition.

The high SiO_2 content of the bauxite facies is a result of weak lateritization [8] and the presence of kaolinite [11]. Based on the Al_2O_3–Fe_2O_3–SiO_2 ternary diagram [50], organic-rich and clay-rich bauxite horizons show weak and moderate lateritization, respectively, whereas oolitic, pisolitic and iron-rich

bauxites plot in the strong lateritization field (Figure 6). Furthermore, the Dopolan bauxite samples plot in the bauxite and kaolinite bauxite fields on the Al_2O_3–Fe_2O_3–SiO_2 ternary diagram (Figure 7) suggesting tropical paleo-geographic conditions which favored bauxitization and the formation of bauxite horizons [9,51].

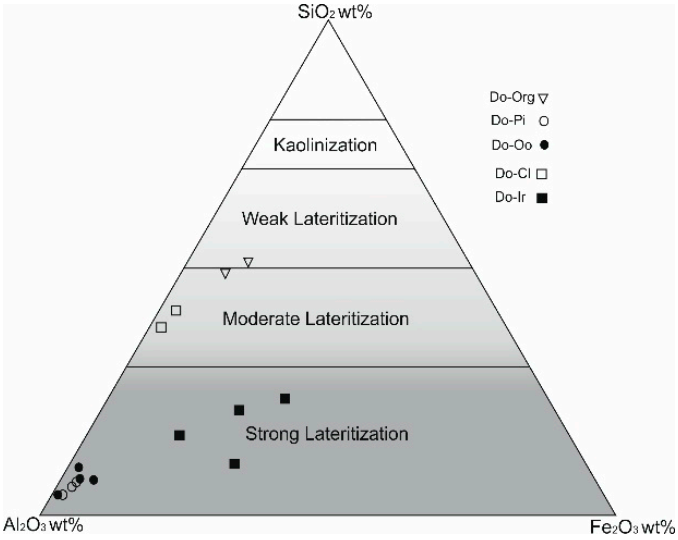

Figure 6. Ternary plot of the SiO_2–Al_2O_3–Fe_2O_3 system (after [50]) showing the intensity of lateritization of the Dopolan bauxites.

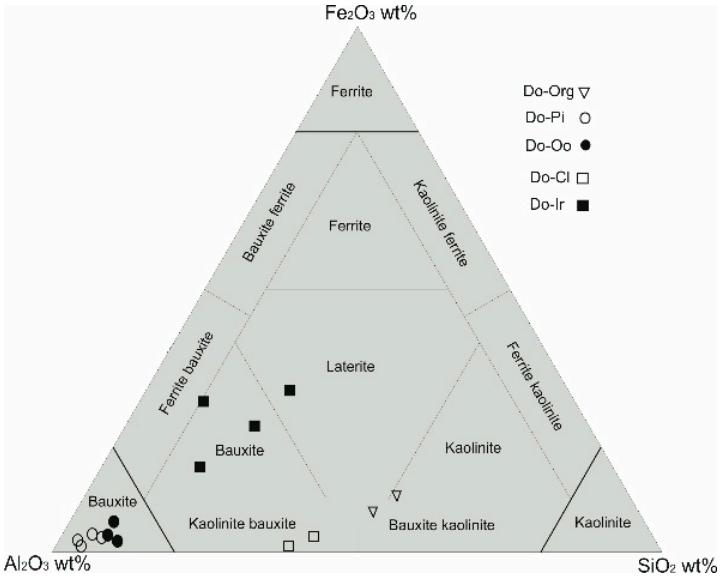

Figure 7. Ternary plot of the SiO_2–Al_2O_3–Fe_2O_3–system (after [52]) showing the Dopolan deposit data.

High content of trace elements such as Cr (132–1088 ppm), Zr (132–557 ppm) and Nb (28–77 ppm) is a significant and common feature of the Dopolan bauxite (Table 2). Trace elements such as Cr, Ni, V, Co, Zr are considered bauxitophilic [53] and they are used in geochemical calculations such as mass change and identification of parent rocks. Trace elements such as Zr, V, and Ga are enriched in all parts of the bauxite; these trace elements are low in the Khaneh–Kat Formation. Zr, Hf, Nb and Ta are immobile elements and show positive correlations (R^2 = 0.64 to 0.87) with TiO_2 (Figure 8).

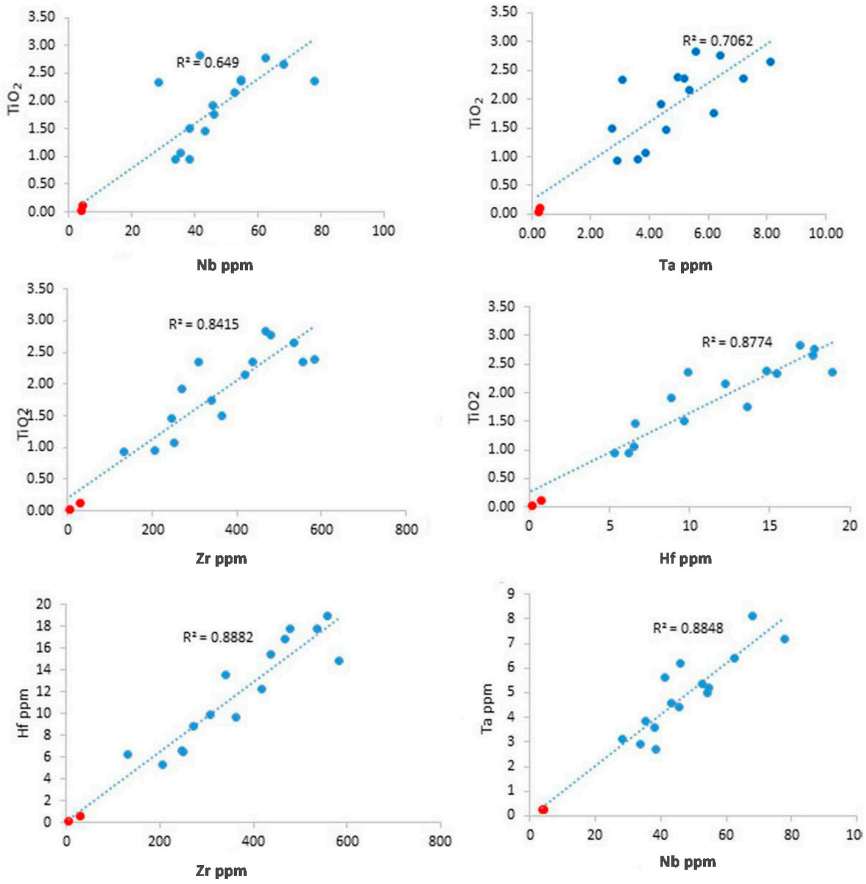

Figure 8. Variation diagrams showing correlations between TiO_2 and trace elements in the Dopolan bauxite deposit. Red circles are carbonate samples, blue circles are bauxite samples.

5.2. Rare Earth Elements

The chondrite-normalized REE diagram of the bauxite horizons and argillitic dolomite from the Khaneh–Kat Formation shows a similar pattern with light rare earth element (LREE) enrichment and heavy rare earth element (HREE) depletion and a negative Eu anomaly (Figure 9).

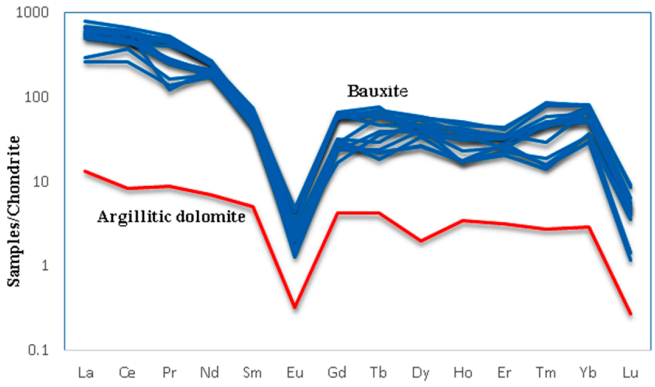

Figure 9. Chondrite-normalized rare earth element (REE) patterns of the bauxite samples as well as argillitic dolomite from the Khaneh–Kat Formation.

The ∑REE of bauxite samples vary from 480 to 1140 ppm (Table 3). There is also a decreasing trend in ∑REE in the bauxite profile from the pisolitic bauxite (1037 ppm) to the iron-rich bauxite (890 ppm). The organic-rich bauxite contains low ∑REE values (522 ppm) (Table 3).

Table 3. Rare earth element composition of samples from the Dopolan bauxite deposit.

Element (ppm)	IR-1	IR-2	IR-3	IR-4	Cl-1	Cl-2	Oo-1	Oo-2	Oo-3	Oo-4	Pi-1	Pi-2	Pi-3	Org-1	Org-2	Kha	Ny	Ch.
La	187.23	177.43	199.32	168.85	164.56	170.59	199.07	168.32	173.80	148.79	198.90	242.30	210.20	88.40	82.12	4.18	4.31	0.310
Ce	489.44	479.65	386.09	389.69	367.88	376.46	434.65	347.40	456.36	343.22	428.10	532.20	480.04	287.90	209.95	6.82	14.90	0.808
Pr	32.30	14.60	33.51	34.23	32.03	30.16	59.40	55.71	54.60	48.97	52.09	64.08	54.57	19.30	16.69	1.09	3.22	0.122
Nd	122.26	131.35	119.91	114.71	123.71	109.27	148.40	156.23	144.75	159.31	146.69	161.28	150.12	108.33	105.56	4.25	2.80	0.600
Sm	9.25	8.29	10.93	9.04	10.54	12.31	13.01	11.67	10.42	11.76	14.33	12.09	13.43	8.67	8.48	0.98	2.85	0.195
Eu	1.73	1.18	0.95	1.53	1.13	1.98	2.28	3.25	2.51	3.35	3.21	3.52	3.44	1.45	1.51	0.24	0.30	0.073
Gd	4.25	8.13	5.83	7.32	7.36	8.38	16.21	14.70	15.38	15.66	14.31	16.13	16.71	7.01	6.25	1.10	3.77	0.259
Tb	1.65	1.37	1.84	2.73	1.04	0.87	2.76	2.91	2.81	2.20	3.22	3.25	3.58	1.03	1.13	0.20	0.43	0.047
Dy	14.59	18.40	12.47	13.95	8.65	10.95	13.41	14.31	17.48	14.36	18.68	18.23	10.85	8.12	13.03	0.65	2.62	0.322
Ho	2.98	2.57	2.16	1.21	1.23	1.24	2.29	2.28	2.73	2.81	3.32	3.67	2.21	1.26	1.64	0.25	0.52	0.071
Er	6.80	5.14	6.53	5.88	4.32	4.74	7.09	7.08	7.22	7.48	8.99	8.72	6.84	5.74	5.34	0.67	1.37	0.210
Tm	1.47	1.52	1.63	1.64	0.46	0.61	2.51	1.54	1.43	0.92	2.67	2.83	1.84	0.48	0.51	0.09	0.18	0.032
Yb	10.36	10.40	11.37	11.04	7.78	7.36	16.38	15.67	14.21	14.34	16.70	16.30	13.10	6.00	7.41	0.61	1.10	0.209
Lu	1.41	1.51	1.62	1.71	1.28	1.15	1.40	1.40	1.60	2.02	2.71	2.93	1.78	0.38	0.47	0.09	0.16	0.032
Y	47.10	57.20	58.10	55.30	42.70	36.26	55.20	58.64	43.10	36.06	65.18	61.21	47.46	27.36	27.40	6.97	13.60	-
ΣREE	932.82	918.74	852.26	818.83	774.67	772.33	974.06	861.11	948.40	811.25	979.10	1148.74	1016.17	571.43	487.49	27.19	52.13	4.24
La/Yb	18.07	17.06	17.53	15.29	21.15	23.18	12.15	10.74	12.23	10.38	11.91	14.87	16.05	14.73	11.08	6.85	3.92	1.48
Eu/Eu *	0.08	0.04	0.04	0.06	0.04	0.06	0.05	0.08	0.06	0.08	0.07	0.08	0.07	0.06	0.06	0.07	0.03	38.77
Ce/Ce *	1.73	1.68	1.33	1.49	1.38	1.47	1.35	1.14	1.54	1.19	1.34	1.44	1.44	1.57	1.20	0.86	2.29	1.09

Eu/Eu * = $(Eu\cdot n)/\sqrt{(Sm\cdot n)\times(Gd\cdot n)}$. Ce/Ce * = $Ce\cdot n/\sqrt{(La\cdot n)\times(Nd\cdot n)}$. Chondrite values are from Boynton, 1984 [54]. Ny = Nyriz Formation, Ch. = Chondrite.

The ∑REE content of the Kaneh–Kat Formation (27 ppm) is within the average range of carbonate rocks (23–27 ppm; [46]. Iron-rich and clay-rich bauxites with the lowest content of ∑REE the carbonate bed rock. Enrichment of LREEs in the bauxitic zone is a result of authigenic processes [13].

The chondrite-normalized REE patterns of different bauxite horizons and Khaneh–Kat Formation show similar patterns with negative Eu anomalies (0.04–0.08; Table 3). All sequences of the bauxites and bedrock (Khaneh–Kat dolomite) display negative Eu anomalies. Eu/Eu * anomalies in all bauxite horizons show that this ratio is conservative. Variations of La/Y ratio in the bauxites have been used for determining change in pH during weathering [11,13,55]; values of La/Y < 1 imply prevalence of acidic conditions whereas values of La/Y > 1 indicate basic conditions (Figure 10). Calculated La/Y variations in bauxites can be related to LREE variations in the bauxite profile suggesting that the leaching of LREE in the pisolitic bauxite may be the result of low pH conditions. Ce/Ce * ratio in the 0.86–1.73 range (Table 3) suggests that Ce^{+3} was leached out from the oolitic and pisolitc bauxite and was available to be transported to deeper layers and precipitated near the bed rock [15].

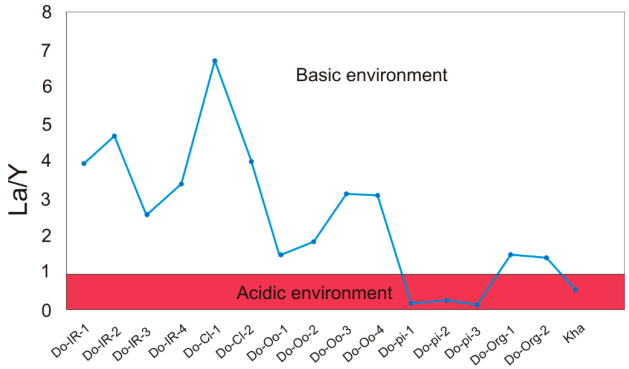

Figure 10. La/Y ratios from the Khaneh–Kat Formation and bauxite samples of the Dopolan deposit [13,55].

5.3. Protolith

The Cr-Ni binary diagram can be used to predict the protolith of the bauxite deposit [2,11,22,56]; Dopolan samples plot in the karst bauxite field (Figure 11). Karst bauxites form on a variety of parent rocks such as carbonates, rock debris, volcanic ash, and wind-born material [22]. To identify the protolith of the Dopolan bauxite, calculated correlation coefficients of major elements are used. The strong positive correlation between Ti and Al in the Dopolan deposit suggests a relationship between the bauxite horizons and the argillitic dolomite of the Khaneh–Kat Formation (Figure 12).

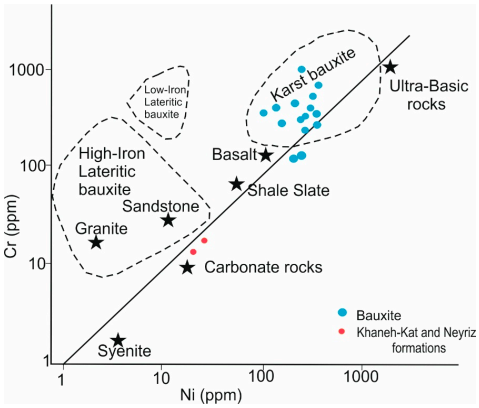

Figure 11. Binary diagram of Cr *versus* Ni to imply parent rock (after [2,11,22,56]). The Dopolan data plot in the karst bauxite field. The Khaneh–Kat data plot near the carbonate rocks.

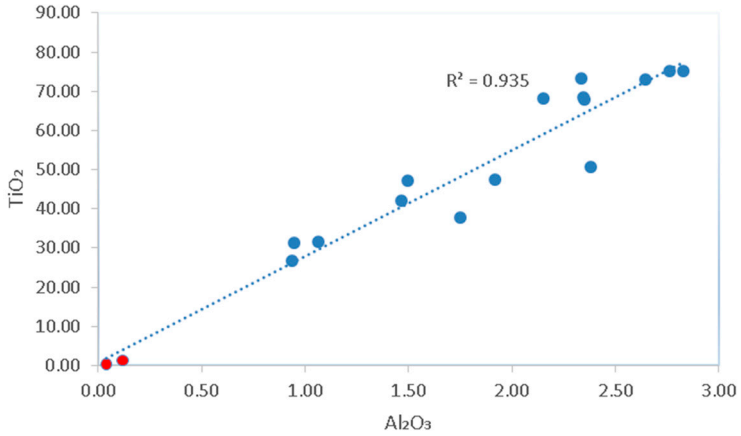

Figure 12. Scatter plot of TiO_2 *versus* Al_2O_3 in the Dopolan deposit. Red circles are carbonate samples, blue circles are bauxite samples.

5.4. Mass Change

Mass change is associated with enrichment or depletion of elements during bauxitization [2,10,14]. The content of immobile elements in relatively fresh (parent) rock and weathered rocks can be used to calculate mass changes during weathering. In the residual accumulated bauxite ore, elements such as Ti, Zr, Hf, Nb, Ta, Cr and Ni are considered to be relatively immobile. Loss and/or gain in mass of the weathered Dopolan profiles were calculated based on Ti, which is strongly immobile during weathering of bauxite [14]. These calculations are based on Maclean [57] expression: where $EF = TiO_{2protolith}/TiO_{2bauxite}$ (Table 4), RC = % component in altered rock × EF (Table 4); and MC = RC − precursor composition (Table 5).

Table 4. Calculated enrichment factor (EF) and reconstructed compositions (RC, in wt %) of samples from bauxite profiles of the Dopolan deposit.

Samples	Do-IR-1	Do-IR-2	Do-IR-3	Do-IR-4	Do-Cl-1	Do-Cl-2	Do-Oo-1	Do-Oo-2	Do-Oo-3
EF	1.006	0.732	1.202	1.015	1.067	1.348	1.324	1.452	1.392
SiO_2	10.020	30.842	17.022	15.300	37.520	27.271	7.048	4.927	4.887
Al_2O_3	58.398	59.888	43.754	63.753	50.399	43.376	64.526	58.793	59.231
Fe_2O_3	27.346	40.279	19.113	15.136	2.753	0.869	1.450	2.146	3.948
K_2O	0.703	2.211	0.716	1.151	0.846	0.308	0.285	0.564	0.690
MnO	0.017	0.039	0.013	0.000	0.002	0.000	0.002	0.001	0.001
Na_2O	0.019	0.026	0.016	0.081	0.014	0.012	0.013	0.017	0.012
P_2O_5	0.139	0.172	0.093	0.095	0.064	0.060	0.095	0.061	0.078
MgO	0.392	1.109	0.425	0.569	0.106	0.240	0.047	0.360	0.086
TiO_2	2.040	2.040	2.040	2.030	2.040	2.040	2.040	2.040	2.040

Al_2O_3 is enriched in the bauxite horizons especially in the pisolitic and oolitic bauxite (Figure 13). Iron enrichment in the iron-rich bauxite is due to the presence of pyrite, whereas all other bauxite horizons show Fe depletion. The highest Si enrichment is seen in the organic-rich bauxite which is related to the Eh–pH conditions and the presence of clay minerals. Ca, K, Na and P_2O_5 were leached out of weathering protolith whereas Al was enriched in the residual debris.

Table 5. Mass changes (in %) of the Dopolan samples based on the reconstructed compositions (RC, in wt %).

Samples	Do-IR-1	Do-IR-2	Do-IR-3	Do-IR-4	Do-Cl-1	Do-Cl-2	Do-Oo-1	Do-Oo-2	Do-Oo-3	Do-Oo-4	Do-Pi-1	Do-Pi-2	Do-Pi-3	Do-Org-1	Do-Org-2
SiO_2	−34.47	−13.65	−27.47	−29.19	−6.97	−17.22	−37.44	−39.56	−39.60	−42.03	−41.12	−39.74	−42.20	30.27	32.65
Al_2O_3	42.48	43.97	27.84	47.83	34.48	27.46	48.61	42.87	43.31	40.19	38.13	47.94	39.44	50.82	41.87
Fe_2O_3	−3.00	9.93	−11.24	−15.21	−27.60	−29.48	−28.90	−28.21	−26.40	−29.65	−28.72	−28.32	−29.35	−18.51	−14.13
K_2O	−3.72	−2.22	−3.71	−3.28	−3.58	−4.12	−4.14	−3.86	−3.74	−3.50	−4.24	−3.00	−4.21	4.29	3.91
MnO	−0.53	−0.51	−0.54	−0.55	−0.55	−0.55	−0.55	−0.55	−0.55	−0.55	-0.55	−0.55	−0.53	−0.48	−0.55
Na_2O	−1.21	−1.20	−1.21	−1.14	−1.21	−1.21	−1.21	−1.21	−1.21	−1.17	−1.21	−1.19	−1.18	−1.11	−0.96
P_2O_5	−0.80	−0.76	−0.84	−0.84	−0.87	−0.88	−0.84	−0.87	−0.86	−0.87	−0.84	−0.83	−0.82	−0.81	−0.83
MgO	0.39	1.11	0.42	0.57	0.11	0.24	0.05	0.36	0.09	0.18	0.01	0.03	0.25	0.68	1.98
TiO_2	0.00	0.00	0.00	−0.01	0.00	0.00	0.00	0.00	0.00	0.00	0.00	0.00	0.00	0.00	0.01
∑Mc	−0.86	36.67	−16.74	−1.82	−6.19	−25.76	−24.43	−31.03	−28.96	−37.38	−38.55	−25.66	−38.61	65.15	63.95

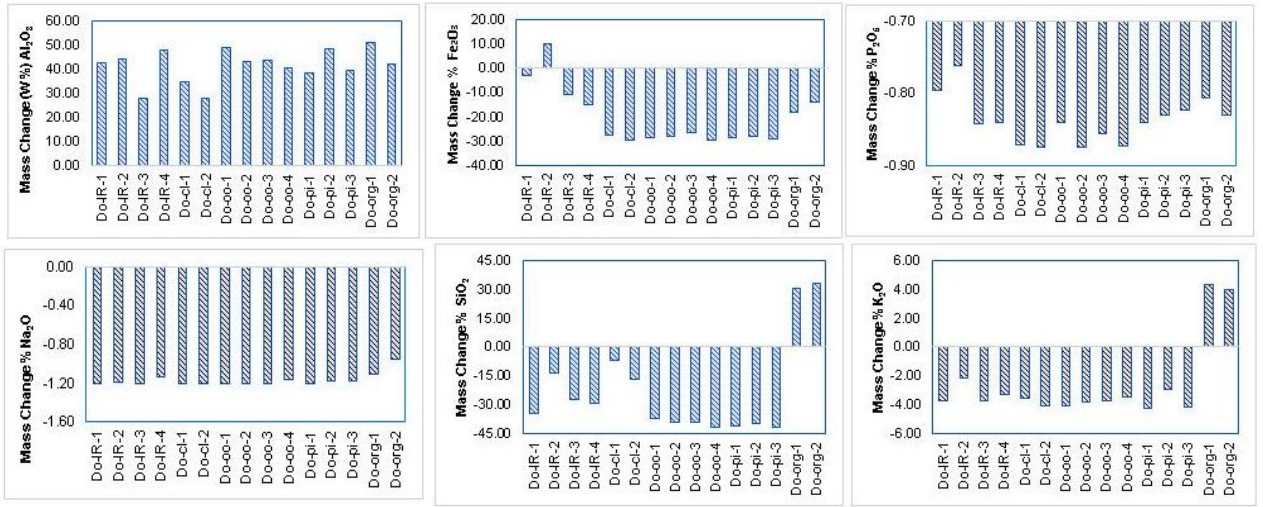

Figure 13. Mass changes in the Dopolan bauxite deposit relative to the Khaneh–Kat argillitic dolomite. The mass changes can be considered as enrichment and depletion in weight % or grams per 100 g of the argillic dolomite precursor.

5.5. Isotopic Signatures

The geochemical characteristics of O and D isotopes have been widely used to study bauxitization processes and paleo-climate changes (e.g., [58]). Hydroxyl (OH) bearing minerals such as kaolinite and boehmite are considered to be one of the main controls on the isotopic composition of bauxite deposits [28].

Oxygen and hydrogen isotope compositions of the footwall dolomite (Khaneh–Kat Formation) are +28.8‰ and −59.7‰, respectively (Table 6). $\delta^{18}O$ and δD values of various bauxite horizons range from +7.63‰ to +9.35‰ and −66.49‰ to −49.91‰, respectively (Table 6 and Figure 14). One sample from the calcite cement of the footwall dolomite shows $\delta^{13}C$ value of −7.34‰ (Table 6). Such depleted $\delta^{13}C$ values are considered to reflect subaerial exposure and influence of the karstification associated with the unconformity surface [48].

Table 6. Stable isotope composition of selected samples from the Dopolan bauxite deposit.

Samples	$\delta^{18}O_{SMOW}$ (‰)	δD_{SMOW} (‰)	$\delta^{13}C_{PDB}$ (‰)
D-1 (Iron-rich bauxite)	8.74	−49.91	-
D-2 (Clay-rich bauxite)	8.37	−66.49	-
D-3 (Oolitic bauxite)	7.63	−56.65	-
D-4 (Pisolitic bauxite)	7.89	−54.77	-
D-5 (Organic-rich bauxite)	9.35	−60.59	-
D-6 (Khaneh–Kat Formation)	28.85	−59.69	−7.34

PDB = Pee Dee Belemnite.

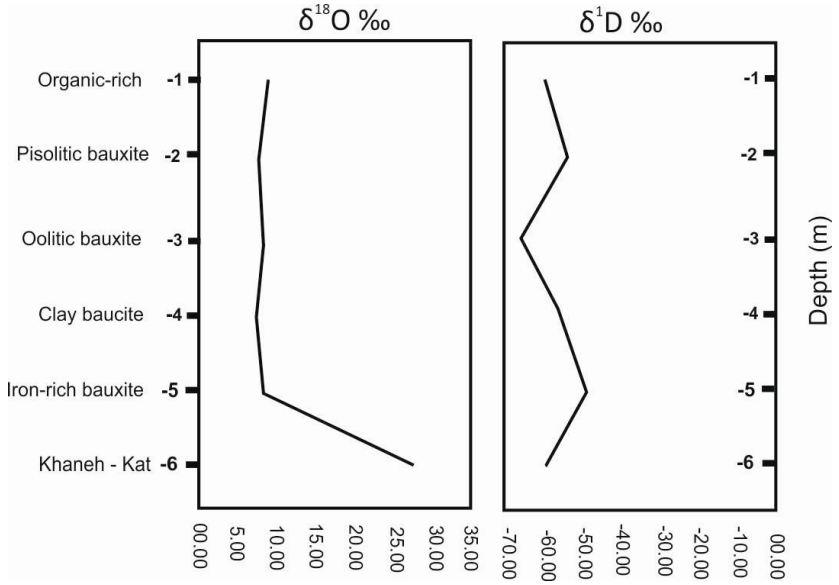

Figure 14. Vertical variation of the $\delta^{18}O$ and δD values of the Dopolan and the Khaneh–Kat Formation.

Calcite from the footwall dolomite (Khaneh–Kat Formation) plots away from the kaolinite line ($\delta D = 7.55\delta^{18}O - 219$); [59]; Figures 15 and 16). The Dopolan bauxite samples plot close to the boehmite line (Figure 15). Homogenous isotopic compositions of these samples indicates a relatively constant isotope composition during the development of bauxite horizons and remobilization of Al (secondary boehmite [30]).

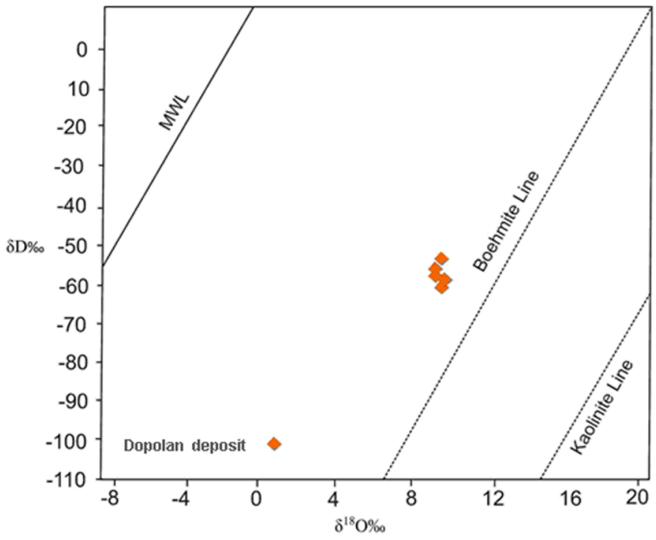

Figure 15. Isotope composition of bauxite horizons of the Dopolan deposit. Kaolinite line after [59]; boehmite line after [29]. MWL, Meteoric water line. SMOW, Standard mean ocean water.

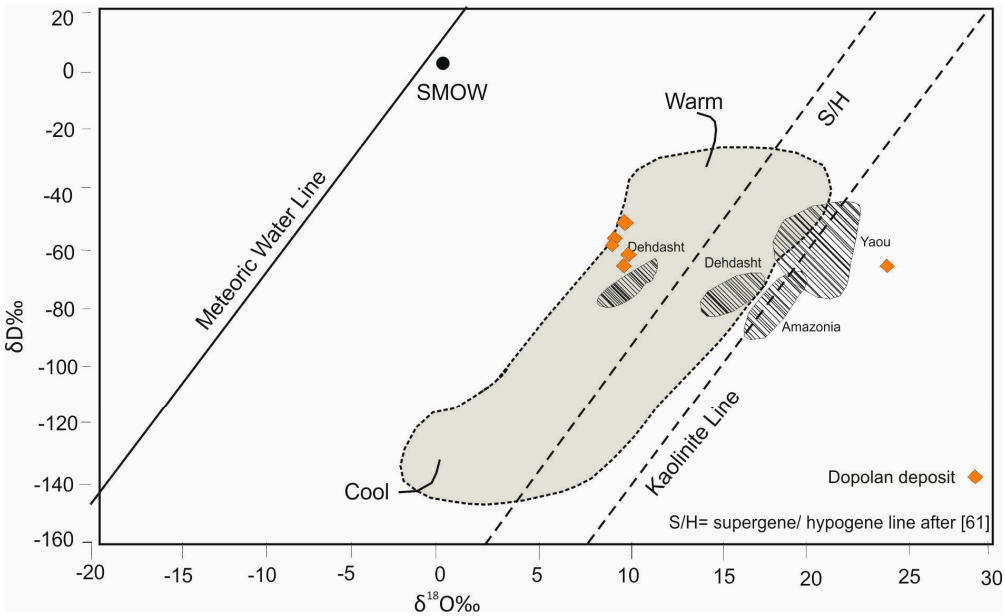

Figure 16. $\delta^{18}O$ and δD values of the Dopolan kaolinite compared with data from Amazonia (after [60]), Yaou (after [58]) and Dehdasht after [27]. Kaolinite line (after [59]). SMOW = Standard Mean Ocean Water; S/H = supergene/hypogene line after [61].

6. Discussion

In karstic terranes, soluble bedrocks such as limestone and dolomite are dissolved by CO_2-enriched water. Karstification creates space for bauxite deposition. Bauxite accumulated in the karst cavities is more protected from erosion compared to regolith on silicate rocks [11,62]. Such a process leads to the formation of a specific type of karst called ore karst which occurs only on the exokarst floor [63]. The term was used in carbonate rocks wherein the ore was developed due to dissolution of carbonates by acidic fluids related to oxidation of sulfide ores [63]. Mineralogy, karst characteristics, wall–rock relationship, and geological setting indicate that the Triassic Dopolan bauxite deposit formed in a karstic environment. Boehmite, diaspore, kaolinite, nacrite, pyrite, anatase and rutile are common minerals. The matrix type suggests an authigenic origin for bauxite; however,

terrigenous grains such as intraclasts, ooids and erosional ooid nucleus imply a semi-authigenic origin, at least for part of the deposit. Also, the presence of angular bauxite and detrital phases indicates some displacement into or within the karstic area. Gibbsite can transform to boehmite in surface environments and boehmite can transform to diaspore in a near-surface environment [18,64–67]. Kaolinite and other clays such as nacrite can also be present in bauxite deposits [53]. The pisolitic texture results from aggregation of discolored pisolites showing evidence of deferrification process. Deferrification in pisolitic bauxites may be controlled by organic ligands which affect the solubility and dissolution of iron oxides [7]. Micro-organisms can also reduce Fe^{3+} to Fe^{2+} in solutions to provide energy for metabolism potentially leading to deferrification [68]. The organic ligands could have also contributed to the formation of acidic (pH between 3 and 6) and reducing conditions which prevailed during bauxitization in the Dopolan area.

Trace element composition (e.g., Cr, Ni; Figure 11) show that the Dopolan deposit is a karst bauxite type which located in the Zagros Fold-Thrust Zone. The Zagros fold-thrust belt contains the most important sedimentary basins in Iran, wherein sedimentary rocks reach depths of more than 12 km and are comprised mainly of carbonate and detrital sediments. The lack of magmatic units suggests that the Khaneh–Kat argillic dolomite can be considered as the likely parent rock for the Dopolan bauxite deposit. The similarity of REE pattern of bauxite horizons and the Khaneh–Kat argillic dolomite support that the Khaneh–Kat could be parent rock of the Dopolan bauxite [69]. Furthermore, the REEs show affinity to mobilization during bauxitization and subsequent redistribution [15]. The REE patterns demonstrate that bauxite samples are enriched in REEs, possibly due to prolonged tropical weathering which led to the breakdown of rock-forming minerals [70,71].

Minor REE variations across the bauxite horizons probably reflect Eh and pH fluctuations during formation of each horizon [72]. Mobility of LREEs depends on pH variation in the bauxite profile in the weathering system. Variations of La/Y ratio in bauxite have been used to study pH change during weathering [11,13]; values of $La/Y < 1$ imply prevalence of acidic conditions whereas values of $La/Y > 1$ indicate basic conditions (Figure 10). Iron-rich, clay-rich, oolitic, and organic-rich bauxite horizons of Dopolan are enriched in LREEs suggesting high pH conditions during formation of these bauxites (Figure 10). However, the pisolitic bauxite is depleted in LREEs possibly reflecting low pH conditions during formation (Figure 10). The acidic solutions probably resulted from weathering of pyrite which explains HREEs' enrichment in the pisolitic bauxite [73].

Positive correlation between REEs and some major elements implies that the REEs are hosted in the specific minerals (Table 7) or both REEs, and major elements have been enriched by the same processes. In the Dopolan deposit, Ti has positive correlation with all REEs (Table 7) which probably suggests that distribution of REE is controlled by the formation of authigenic heavy minerals such as rutile and anatase [74]. The strong positive correlations (R = 0.71–0.80) between HREEs and Al_2O_3 suggest (Table 7) that they may be hosted by Al oxides (e.g., diaspore and boehmite minerals) or their relative content increased during bauxite formation processes.

In addition, variation in the amount of pyrite, organic matter and other minerals such as oxyhydroxides, phosphates and Fe oxides in the weathering profile can affect Eh–pH conditions under wet-tropical environments [7,13,75,76]. The mass change calculations of the bauxite horizons show that Ca, K and P_2O_5 were largely leached out of the weathering system whereas Al was enriched in the residual system. The bauxitization at Dopolan occurred along a karstification surface between the Khaneh–Kat and Neyriz Formations. Due to high CO_2 and temperature [77], continental weathering was intense during this time period. The depleted $\delta^{13}C$ value (−7.34‰) supports this hypothesis that the Khaneh–Kat Formation has experienced post-depositional isotope exchange with meteoric waters during the karstification process. Similar to the Early Permian Australian bauxite deposits, the oxygen and hydrogen isotopic compositions of the Dopolan bauxite fall close to the boehmite line (Figures 15 and 17). The Dopolan kaolinite plots on the left of the kaolinite line and the supergene/hypogene line (S/H; Figure 17) indicating kaolinite equilibrium with meteoric water and supports the supergene origin for kaolinite. Furthermore, the isotopic composition of kaolinite (Figure 16) shows that the

deposit formed under a warm climate. This climate is consistent with the results of Wang *et al.* [41] who, based on the carbon-isotope compositions of calcite in the Khaneh–Kat Formation, inferred a warm climate during Permo–Triassic time.

Table 7. Correlation coefficients of REEs and some major and trace elements of the Dopolan bauxite deposit.

Element/Oxide	Al_2O_3	Fe_2O_3	TiO_2	P_2O_5	Zr	Nb	Hf	Th
La	0.83	0.18	0.82	0.85	0.77	0.64	0.77	0.79
Ce	0.83	0.28	0.75	0.85	0.73	0.66	0.71	0.74
Pr	0.82	−0.28	0.90	0.77	0.79	0.70	0.84	0.80
Nd	0.90	0.04	0.86	0.77	0.77	0.79	0.78	0.77
Sm	0.91	−0.12	0.93	0.79	0.84	0.76	0.85	0.84
Eu	0.92	−0.37	0.87	0.76	0.75	0.64	0.80	0.75
Gd	0.92	−0.41	0.84	0.72	0.77	0.68	0.81	0.78
Tb	0.87	−0.13	0.78	0.83	0.68	0.57	0.76	0.73
Dy	0.71	0.30	0.66	0.69	0.64	0.56	0.65	0.63
Ho	0.75	0.18	0.68	0.80	0.60	0.50	0.67	0.60
Er	0.88	0.04	0.82	0.81	0.73	0.66	0.78	0.72
Tm	0.72	0.10	0.64	0.83	0.55	0.32	0.61	0.60
Yb	0.92	−0.02	0.85	0.80	0.75	0.67	0.79	0.77
Lu	0.82	−0.00	0.80	0.81	0.73	0.46	0.79	0.73
Y	0.72	0.29	0.69	0.75	0.59	0.47	0.60	0.613

Such paleo-climatic conditions in this part of the High Zagros Mountain favored bauxitization, causing mobilization and enrichment of aluminum. Geochemical composition, stratigraphic evidence, and texture/mineralogy show that dolomite from the Khaneh–Kat Formation was protolith for the bauxite deposit at Dopolan. The REE pattern of the Dopolan bauxite horizons reflects enrichment in LREE in the bauxite zone of an authigenic origin. Enrichment and depletion of elements were strongly influenced by the pH of solution; low pH favored leaching and high pH favored enrichment of elements in the bauxite horizons.

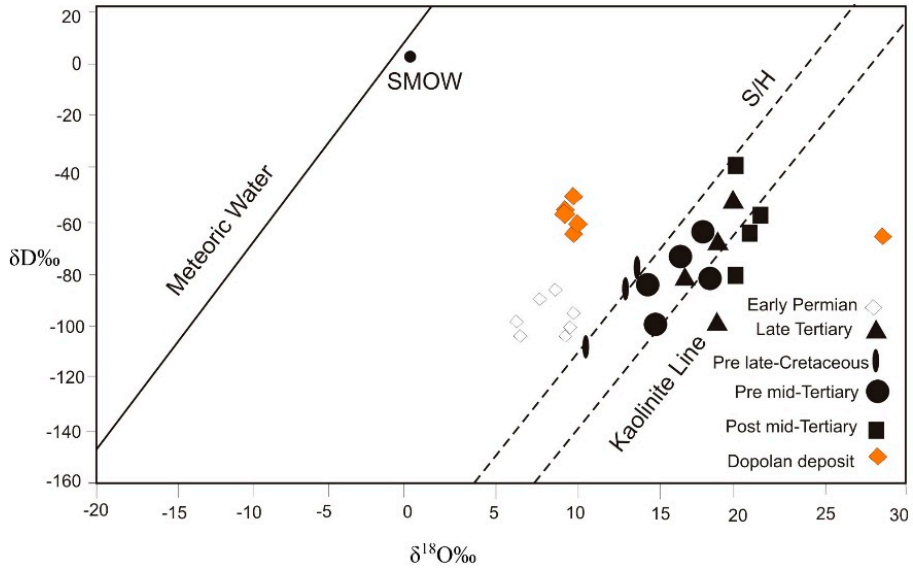

Figure 17. Relationship between $\delta^{18}O$ and δD values for clay minerals from Australian regolith profiles (Data from [78] and the Dopolan kaolinite. SMOW, Standard mean ocean water; S/H = supergen/hypogene kaolinite line from [61]; Kaolinite line from [59].

7. Conclusions

The following conclusions can be made based on the data obtained from the Dopolan deposit.

1. Field observation and geochemical data suggest that the Dopolan bauxite deposit (in the Zagros sedimentary basin) is a karst bauxite type and originated from the argillitic dolomite of the Khaneh–Kat Formation.

The main mineral assemblage of this deposit consists of diaspore, boehmite, and kaolinite. Oolitic, pisolitic, pelitomorphic, microcrystalline and microgranular are the most important textures. These textures suggest an authigenic origin for the deposit. However, the presence of angular bauxite, detrital phases, pelitomorphic and fluidal textures indicates some small displacement into or within the karstic area.

2. Mass change calculation shows silica dissolution and deferrification in the bauxite horizons, causing Al-enrichment and bauxite formation.

3. The chondrite-normalized REE patterns of the different bauxite horizons and the Khaneh–Kat dolomite are similar, which may suggest that the Khaneh–Kat dolomite is the parent rock. The REEs are most enriched in the pisolitic and oolitic bauxite which is located in the upper part of the bauxite horizon and lie within the strong laterization. Minor REE changes across the bauxite profile probably reflect Eh and pH variations in the bauxitic profile.

4. The Dopolan deposit shows a relatively constant isotopic condition during the development of bauxite horizons and remobilization of Al. The $\delta^{18}O$ and δD values of kaolinite samples suggest kaolinite equilibrium with meteoric water which supports a supergene origin.

5. The $\delta^{13}C$ value (−7.34‰) of Khaneh–Kat formation is lower than the values of normal Triassic carbonates (−1‰–+5‰): thus supporting that the Khaneh–Kat Formation experienced post-depositional isotope exchange with organic carbon by meteoric water during karstification processes.

Acknowledgments: All financial support for this research was provided by the Research Office at Shiraz University, Iran. We thank all staff of this office for their support. The CEO of the Dopolan bauxite mine is thanked for providing unlimited access to the Dopolan deposit. Mohammad Ali Mackizadeh (Isfahan University), Mostafa Nejadhadad (Shiraz University), and Maryam Khodadadi (Shiraz University) are thanked for their help during field work. The authors are also grateful to the anonymous reviewers of the journal of Minerals for their constructive comments.

Conflicts of Interest: The authors declare no conflict of interest.

References

1. Dill, H. The "chessboard" classification scheme of mineral deposits: Mineralogy and geology from aluminum to zirconium. *Earth Sci. Rev.* **2010**, *100*, 1–420. [CrossRef]
2. Valeton, I.; Biermann, M.; Reche, R.; Rosenberg, F. Genesi of nickel laterites and bauxite, Antalya, Turkey. *J. Asian Earth Sci.* **1987**, *27*, 512–522.
3. Petrascheck, W.E. The genesis of allochthonous karst type bauxite deposits of Southern Europe. *Miner. Depos.* **1989**, *24*, 77–82. [CrossRef]
4. Yaalon, D.H. Soils in the Mediterranean region; what makes them different? *Catena* **1997**, *28*, 157–169. [CrossRef]
5. Oggiano, G.; Mameli, P. The bauxite of North Western Sardinia. *Rend. Semin. Fac. Sci. Univ. Cagliari Suppl.* **2001**, *71*, 59–73.
6. Ji, H.; Wang, S.; Ouyang, Z.; Zhang, S.; Sun, C.; Liu, X.; Zhou, D. Geochemistry of red residua underlying dolomites in karst terrains of Yunnan–Guizhou Plateau. II. The mobility of rare earth elements during weathering. *Chem. Geol.* **2004**, *203*, 1–27. [CrossRef]
7. Laskou, M.; Economou-Eliopoulos, M. The role of microorganisms on the mineralogical and geochemical characteristics of the Parnassos-Ghiona bauxite deposits, Greece. *J. Geochem. Explor.* **2007**, *93*, 67–77. [CrossRef]

8. Mameli, P.; Mongelli, G.; Oggiano, G.; Dinelli, E. Geological, geochemical and mineralogical features of some bauxite deposits from Nurra (Western Sardinia, Italy): Insights on conditions of formation and parental affinity. *Int. J. Earth Sci.* **2007**, *96*, 887–902. [CrossRef]
9. Zarasvandi, A.; Charchi, A.; Carranza, E.J.M.; Alizadeh, B. Karst bauxite deposits in the Zagros mountain belt, Iran. *Ore Geol. Rev.* **2008**, *34*, 521–532. [CrossRef]
10. Zarasvandi, A.; Zamanian, H.; Hejazi, E. Immobile elements and mass changes geochemistry at Sar-Faryab bauxite deposit, Zagros Mountains, Iran. *J. Geochem. Explor.* **2010**, *107*, 77–85. [CrossRef]
11. Zarasvandi, A.; Carranza, E.J.M.; Ellahi, S.S. Geological, geochemical, and mineralogical characteristics of the Mandan and Deh-now bauxite deposits, Zagros Fold Belt, Iran. *Ore Geol. Rev.* **2012**, *48*, 125–138. [CrossRef]
12. Bardossy, G. European Bauxite Deposits. In *Bauxite: Proceedings 1984 Bauxite Sympo-Sium*; Leonard, J., Jr., Ed.; Society of Mining Engineers: New York, NY, USA, 1984; pp. 411–435.
13. Maksimovic, Z.; Panto, G. Contribution to the geochemistry of the rare earth elements in the karst-bauxite deposits of Yugoslavia and Greece. *Geoderma* **1991**, *51*, 93–109. [CrossRef]
14. Maclean, W.H.; Bonavia, F.F.; Sanna, G. Argillite debris converted to bauxite during karst weathering: Evidence from immobile element geochemistry at the Olmedo Deposit, Sardinia. *Miner. Depos.* **1997**, *32*, 607–616. [CrossRef]
15. Muzaffer, M.; Kupeli, S.; Aryk, F.; Ayhan, A.; Zedef, V.; Doyen, A. Rare earth element (REE) geochemistry and genetic implications of the Mortaş bauxite deposit (Seydişehir/Konya–Southern Turkey). *Chem. Erde Geochem.* **2009**, *69*, 143–159. [CrossRef]
16. Boni, M.; Reddy, S.M.; Mondillo, N.; Balassone, G.; Taylor, R. A distant magmatic source for Cretaceous karst bauxites of southern Apennines (Italy), revealed through SHRIMP zircon age dating. *Terra Nova* **2012**, *24*, 326–332. [CrossRef]
17. Mongelli, G.; Boni, M.; Buccione, R.; Sinisi, R. Geochemistry of the Apulian karst bauxites (Southern Italy): Chemical fractionation and parental affinities. *Ore Geol. Rev.* **2014**, *63*, 9–21. [CrossRef]
18. Bardossy, G. *Karst Bauxites: Bauxite Deposits on Carbonate Rocks (Developments in Economic Geology)*; Elsevier: Amsterdam, The Netherlands, 1982.
19. Wang, Q.; Liu, X.; Yan, C. Mineralogical and geochemical studies of boron-rich bauxite ore deposits in the Songqi region, SW Henan, China. *Ore Geol. Rev.* **2012**, *48*, 258–270. [CrossRef]
20. Franceschelli, M.; Puxeddu, M.; Memmi, I. Li, B-rich Rhaetian metabauxite, Tuscany, Italy: Reworking of older bauxites and igneous rocks. *Chem. Geol.* **1998**, *144*, 221–242. [CrossRef]
21. Calagari, A.A.; Abedini, A. Geochemical investigations on Permo-Triassic bauxitehorizon at Kanisheeteh, east of Bukan, West-Azarbaijan, Iran. *J. Geochem. Explor.* **2007**, *94*, 1–18. [CrossRef]
22. Liu, X.; Wang, Q.; Deng, J.; Zhang, Q.; Sun, S.; Meng, J. Mineralogical and geochemical investigations of the Dajia Salento-type bauxite deposits, western Guangxi, China. *J. Geochem. Explor.* **2010**, *105*, 137–152. [CrossRef]
23. Maclean, W.H.; Kranidiotis, P. Immobile elements as monitors of mass transfer in hydrothermal alteration: Phelps dodge massive sulfide deposits, Matagami, Quebec. *Econ. Geol.* **1987**, *2*, 951–962. [CrossRef]
24. Valeton, I.; Schumann, A.; Vinc, R.; Wieneke, M. Supergene alteration since the Upper Cretaceous on alkaline igneous and metasomatic rocks of the Pososde Caldas ring complex, Minas Gerais, Brazil. *Appl. Geochem.* **1997**, *12*, 133–154. [CrossRef]
25. Liaghat, S.; Hosseini, M.; Zarasvandi, A. Determination of the origin and mass change geochemistry during bauxitization process at the Hangam deposit, SW Iran. *Geochem. J.* **2003**, *37*, 627–637. [CrossRef]
26. Bogatyrev, B.A.; Zhukov, V.V. Bauxite provinces of the world. *Geol. Ore Depos.* **2009**, *5*, 339–355. [CrossRef]
27. Hoefs, J. *Stable Isotope Geochemistry*, 6th ed.; Springer-Verlag: Berlin, Germany, 2009; p. 285.
28. Chivas, A.R.; Bird, M.I. Palaeoclimate from Gondwana clays. In *Clays: Controlling the Environment*, Proceeding of the 10th International Clay Conference, Adelaide, Australia, 18–23 July 1993; Churchmann, G.J., Fitzpatrick, R.W., Eggleton, R.A., Eds.; CSIRO Pub: Melbourne, Australia; pp. 333–338.
29. Bird, M.I.; Chivas, A.R. Stable-isotope geochronology of the Australian Regolith. *Geochim. Cosmochim. Acta* **1989**, *53*, 3239–3256. [CrossRef]
30. Zarasvandi, A.; Foroghinia, A.; Pourkaseb, H.; Charchi, A. Stable isotopes geochemistry of the bauxite horizons in the Dehdasht area, Southwest Iran. *Iran. J. Sci. Technol.* **2013**, *37*, 189–197.

31. Smaeli, D.; Rahimpour-Bonab, H.; Esna-Ashari, A.; Kananian, A. Petrography and geochemistry of the Jajarm karst bauxite ore deposit, NE Iran: Implications for source rock material and ore genesis. *Turk. J. Earth Sci.* **2010**, *19*, 1–17.
32. Ehsanbakhash, M. Investigation of the Dopolan Bauxite Deposit. Master's Thesis, Shahid Beheshti University, Tehran, Iran, 1993. (In Farsi).
33. Khodadadi, M.; Taghipour, B. Mineralogy, Geochemistry and Genesis of Dopolan Bauxite Deposit, ChaharMahal and Bakhtiari. Master's Thesis, Shiraz University, Shiraz, Iran, 2014. (In Farsi).
34. Agard, P.; Omrani, J.; Jolivet, L.; Mouthereau, F. Convergence history across Zagros, Iran; constraints from collisional and earlier deformation. *Int. J. Earth Sci.* **2005**, *94*, 401–419. [CrossRef]
35. Berberian, M.; King, G.C.P. Towards a paleogeography and tectonic evolution of Iran. *Can. J. Earth Sci.* **1981**, *18*, 210–265. [CrossRef]
36. Allen, M.; Jackson, J.; Walker, R. Late Cenozoic reorganization of the Arabia–Eurasia collision and the comparison of short-term and long-term deformation rates. *Tectonics* **2004**, *23*. [CrossRef]
37. Egard, P.; Omrani, J.; Jolivet, L.; Whitechurch, H.; Vrielynck, B.; Spakman, W.; Monie, P.; Meyer, B.; Wortel, R. Zagros orogeny: A subduction-dominated process. *Geol. Mag.* **2011**, *148*, 692–725. [CrossRef]
38. Molnar, M. Tertiary Development of the Zagros Mountains. Available online: http://people.uwec.edu/jolhm/Student_Research/Molnar/reports/zagros.pdf (accessed on 29 January 2016).
39. Ricou, L.E.; Braud, J.; Brunn, J.H. Le Zagros. *Mem. h. ser. Soc. Geol. Fr.* **1977**, *8*, 33–52. (In French).
40. Ehsanbakhshe, M.H.; Rahimzadeh, F. *Ardal Map 1; 100000*; Geological Survey and Mineral Exploration: Tehran, Iran, 1996.
41. Wang, W.; Kanob, A.; Okumura, T.; Ma, Y.; Matsumoto, R.; Matsuda, N.; Ueno, K.; Chen, X.; Kakuwad, Y.; Gharaied, M.H.M.; *et al*. Isotopic chemostratigraphy of the microbialite-bearing Permian–Triassic boundary section in the Zagros Mountains, Iran. *Chem. Geol.* **2007**, *244*, 708–714. [CrossRef]
42. Motiei, H. Stratigraphy of Zagros. *Geol. Surv. Iran* **1993**, *1*, 60–151.
43. White, W.B.; White, E.L. *Karst Landforms: Scope and Processes in the Early Twenty First Century*; Elsevier: Amsterdam, The Netherlands, 2013.
44. Parkhiede, H. *Exploration Report North Ridge Argillite ore Bauxite Dopolan*; Institute of Non-Metallic Materials Esfahan: Isfahan, Iran, 1996. (In Farsi)
45. Bird, M.I.; Longstaffe, F.; Fyfe, W.; Bildgen, P. Oxygen-isotope systematics in a multiphase weathering system in Haiti. *Geochim. Cosmochim. Acta* **1992**, *56*, 2831–2838. [CrossRef]
46. Faure, G. *Principles of Isotope Geology*, 2nd ed.; Wiley: Hoboken, NJ, USA, 1986.
47. German-Heins, J. Iron-rich encrustation on the footwall of the Gant bauxite (Vertes Hills, Hungary) evidence for preservation of organic matter under exceptional conditions? *Sediment. Geol.* **1994**, *94*, 73–83. [CrossRef]
48. Hajikazemi, E.; Al-Aasm, S.; Coniglio, M. Subaerial exposure and meteoricdiagenesisof the Cenomanian–Turonian Upper Sarvak formation, Southwestern Iran. *Geol. Soc. Lond.* **2010**, *330*, 253–272. [CrossRef]
49. Delvigne, J.E. *Atlas of Micromorphology of Mineral Alteration and Weathering*; Mineralogical Association of Canada: Quebec, QC, Canada, 1998; p. 494.
50. Schellmann, W. A new definition of laterite. *Mem. Geol. Survey India* **1986**, *120*, 1–7.
51. Alavi, M. Regional stratigraphy of the Zagros fold-thrust belt of Iran and its proforeland evolution. *Am. J. Sci.* **2004**, *304*, 1–20. [CrossRef]
52. Aleva, G.J.J. *Laterites: Concepts, Geology, Morphology and Chemistry*; International Soil Reference and Information Centre (ISRIC): Wageningen, The Netherlands, 1994; Volume 169.
53. Boni, M.; Rollinson, G.; Mondillo, N.; Balassone, G.; Santoro, L. Quantitative mineralogical characterization of karst bauxite deposits in the Southern Apennines, Italy. *Econ. Geol.* **2013**, *108*, 813–833. [CrossRef]
54. Boynton, W.V. Geochemistry of the rare earth elements: Meteorite studies. In *Rare Earth Element Geochemistry*; Henderson, P., Ed.; Elsevier: Amsterdam, The Netherlands, 1984; pp. 63–114.
55. Crnicki, J.; Jurkovic, I. Rare earth elements in Triassic bauxites of Croatia Yugoslavia. *Travaux* **1990**, *19*, 239–248.
56. Schroll, E.; Sauer, D. Beitrag zur Geochemie von titan, chrom, nikel, cobalt, vanadium und molibdan in bauxitischen gestermenund problem der stofflichen herkunft des aluminiums. *Travaux ICSOBA* **1968**, *5*, 83–96.
57. Maclean, W.H. Mass change calculation in altered rock series. *Miner. Depos.* **1990**, *25*, 44–49. [CrossRef]

58. Girard, J.P.; Freyssinet, P.; Chazotu, G. Unraveling climatic changes from intraprofile variation in oxygen and hydrogen isotopic composition of goethite and kaolinite in laterites: An integrated study from Yaou, French Guiana. *Geochim. Cosmochim. Acta* **2000**, *64*, 409–426. [CrossRef]
59. Savin, S.M.; Epstein, S. The oxygen and hydrogen isotope geochemistry of clay minerals. *Geochim. Cosmochim. Acta* **1970**, *34*, 25–42. [CrossRef]
60. Horbe, A.M.C. Oxygen and hydrogen isotopes in pedogenic minerals—Implications for paleoclimate evolution in Amazonia during the Cenozoic. *Geoderma* **2011**, *163*, 178–184. [CrossRef]
61. Sheppard, S.M.F.; Gilg, H.A. Stable isotope geochemistry of clay minerals. *Clay Miner.* **1996**, *31*, 1–24. [CrossRef]
62. Laznika, P. *Giant Metallic Deposits, Future Sources of Industrial Metals*; Springer: Berlin/Heidelbery, Germany; New York, NY, USA, 2006.
63. Andreychouk, V.; Dublyansky, Y.; Ezhov, Y.; Lysenin, G. *Karst in the Earth's Crust: Its Distribution and Principal Type*; University of Silesia: Sosnowiec, Poland, 2009.
64. Ervin, J.S.; Osborn, E.F. The system Al_2O_3–H_2O. *J. Geol.* **1951**, *59*, 381–394.
65. Valeton, I. *Bauxite*; Elsevier: Amsterdam, The Netherlands, 1972; p. 226.
66. Ozlu, N. The trace elements content of karst bauxite and their parent rocks in the Mediterranean belt. *Miner. Depos.* **1983**, *18*, 469–476. [CrossRef]
67. D'Argenio, B.; Mindszenty, A. Bauxites and related paleokarst: Tectonic and climatic event markers at regional unconformities. *Eclogae Geol. Helv.* **1995**, *88*, 453–499.
68. Baskar, S.; Baskar, R.; Kaushik, A. Role of microorganism's in weathering of the Konkan–Goa laterite formation. *Curr. Sci.* **2003**, *85*, 1129–1134.
69. Liu, X.; Wang, Q.; Feng, Y.; Li, Z.; Cai, S. Genesis of the Guangou karstic bauxite deposit in western Henan. *Ore Geol. Rev.* **2013**, *55*, 162–175. [CrossRef]
70. Price, R.G.; Grayc, M.; Wilson, R.E.; Frey, F.A.; Taylor, S.R. The effects of weathering on rare earth elements Y and Ba abundances in Tertiary basalts from southern Australia. *Chem. Geol.* **1991**, *93*, 254–265. [CrossRef]
71. Boulange, B.; Colin, F. Rare earth element mobility during conversion of nepheline syenite into lateritic bauxite at Passa Quatro, Minais Gerais, Brazil. *Appl. Geochem.* **1994**, *9*, 701–711. [CrossRef]
72. Compton, S.J.; White, A.R.; Smith, M. Rare earth element behavior soils and salt pan sediments of a semi-arid granitic terrain in the western Cape, South Africa. *Chem. Geol.* **2003**, *201*, 239–225. [CrossRef]
73. Mucke, A.; Badejoko, T.A.; Akande, S.O. Petrographic-microchemical studies and origin of the Agbaja Phanerozoic Ironstone Formation, Nupe Basin, Nigeria: A product of ferruginized ooidal kaolin precursor not identical to the Minette-type. *Miner. Depos.* **1999**, *34*, 284–296.
74. Koeppenkastrop, D.; de Carlo, E.H. Uptake of rare earth elements from solution by metal oxides. *Environ Sci. Technol.* **1993**, *27*, 1796–1802. [CrossRef]
75. Meshram, R.; Randive, K.R. Geochemical study of laterites of the Jamnagar district, Gujarat, India: Implications on parent rock, mineralogy and tectonics. *J. Asian Earth Sci.* **2011**, *42*, 1271–1287. [CrossRef]
76. Gonzalez Lopez, J.M.; Bauluz, B.; Fernández-Nieto, C.; Oliete, A.Y. Factors controlling the trace-elements distribution in fine-grained rocks: The Albian kaolinite-rich deposits of the Oliete Basin (NE Spain). *Chem. Geol.* **2005**, *214*, 1–19. [CrossRef]
77. Wignall, P.B. Large igneous provinces and mass extinctions. *Earth Sci. Rev.* **2001**, *53*, 1–33. [CrossRef]
78. Pillans, B. Geochronology of the Australian Regolith. Available online: http://crcleme.org.au/RegLandEvol/Geochron_of_%20Aust_Regolith.pdf (accessed on 29 January 2016).